

# Dissipative Soliton Combs with Spectral Filtering

M. Bataille-Gonzalez<sup>a</sup>, M.G. Clerc<sup>a</sup>, B. Kostet<sup>b</sup>, Y. Soupart<sup>b</sup>, and M. Tlidi<sup>b</sup>

<sup>a</sup>Departamento de Física and Millennium Institute for Research in Optics, Facultad de Ciencias Físicas y Matemáticas, Universidad de Chile, Casilla 487-3, Santiago, Chile

<sup>b</sup>Faculté des Sciences, Département de Physique, Université libre de Bruxelles (U.L.B.), C.P. 231, Campus Plaine, B-1050 Bruxelles, Belgium

**Abstract**—The paradigmatic Lugiato–Lefever model describes the electric field envelope in a ring cavity filled with a Kerr medium and driven by a coherent injected laser beam. This model is applied to the formation of frequency combs associated with localized structures in micro- and macro-driven resonators. Including temporal filtering, we derive, in the mean field limit, a generalized Lugiato–Lefever equation. Theoretically, we investigated the formation of periodic and localized structures resulting from the combined action of temporal spectral filtering effect together with Kerr nonlinearity, pumping, dissipation, and frequency detuning. We show that spectral filtering reduces the intensity of the output field and increases the period of traveling solutions. Similarly, the maximum intensity of moving localized structures, often called dissipative solitons, is reduced. In addition, we show that the threshold associated with breathers is shifted toward large input intensities and that the associated domain of existence is significantly reduced. Finally, we analyze the homoclinic bifurcation associated with the formation of localized structures.

**Index Terms**—Modulational instability, dissipative solitons, Kerr combs, temporal spectral filtering

## I. INTRODUCTION

FREQUENCY combs generated by continuous-wave (CW) laser output in microcavity Kerr resonators have revolutionized many fields of science and technology [1]–[3]. Hänsch is credited with being the first to introduce and develop optical frequency combs. These are equally spaced coherent spectral lines [4]. Much attention has been paid to the formation of frequency combs associated with forming Kerr dissipative solitons (DS) of light that maintain their shape during propagation in optical microcavities [5], [6]. This simple optical device has a compact size, a high-quality factor, and allows for chip-scale production of frequency combs [7]–[10]. Kerr–Raman optical frequency combs were also experimentally observed [11]–[16].

From a fundamental point of view, the Lugiato–Lefever equation (LLE) [17] has led to the prediction and analysis of various phenomena, including the theoretical study of Kerr optical frequency comb generation using whispering gallery mode cavities or integrated ring resonators [18]. In particular, frequency combs as the spectral content of localized light structures were theoretically predicted in driven Kerr resonators before their invention [19], [20]. The link between these two objects in micro- and macro-resonators has been established in [21], [22] (See the review [23] in the theme issue [24]). Dissipative solitons are not necessarily stationary. They can exhibit temporal motion or oscillation. In particular, several mechanisms leading to their movement have been

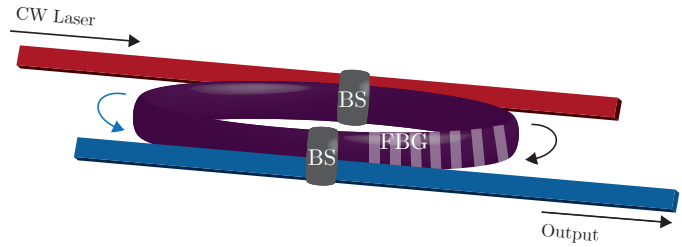


Fig. 1. Schematic setup of a driven ring resonator filled with Kerr media with the filter and driven by a coherent injected field. BS denotes a beam splitter, FBG is a fiber Bragg grating. The arrows account for the direction of light propagation.

described in the literature. It has been shown that uniform soliton motion can be induced by Raman scattering [25]–[27], odd orders of dispersion [28], delayed feedback [29], or spectral filtering [30]–[34].

The aim is to study the generation of dissipative soliton Kerr-combs under the influence of spectral filtering. We consider an optical cavity filled with a Kerr medium, driven by a coherent injected field, and with the inclusion of a temporal spectral filter (see Fig. I). Using a mean-field approximation, we reduce an infinite discrete map (Ikeda map) to the well-known Lugiato–Lefever equation with spectral filtering. A general filter transfer function is used for this derivation. We show that spectral filtering not only affects the coefficient of the second derivative but also produces a first derivative, whose coefficient is purely imaginary. In the second part, we study frequency combs, which are the spectral content of moving dissipative solitons. These solutions are generated due to the subcritical nature of the modulation instability. In this regime, the system undergoes a hysteresis loop involving the periodic moving and stable CW solutions. Moving dissipative solitons do not require bistability between the CW solutions and can be formed in the monostable regime (coexistence regime). We show that spectral filtering reduces the stability domain of the dissipative solitons. In the bistable regime, as the injected field increases, the system transitions from regular moving solitons to moving breathing ones. We show that the spectral filtering shifts this transition towards large input intensities and hence stabilizes a regular motion of moving dissipative solitons. Finally, using a continuation algorithm, we show that the dissipative solitons form an isola that is not associated with a modulational instability threshold. This effect is attributed to

spectral filtering, which breaks the reflection symmetry.

This paper is organized as follows. After briefly presenting a driven Kerr ring resonator with spectral filtering, we derive the mean field model, the generalized LLE (Sec. II). We present the linear stability analysis of the CW solutions and the temporal periodic structures that emerge from the modulational instability (Sec III). Regular moving dissipative structures are then evidenced in the subcritical modulational instability regime, along with their bifurcation diagrams for the monostable and bistable regimes (Sec. IV. A). The results of the continuation algorithm, which captures the homoclinic snaking bifurcation and isolas associated with dissipative solitons, are presented in Sec. IV. B. We conclude in Sec. V.

## II. LUGIATO–LEFEVER EQUATION WITH SPECTRAL FILTERING

### A. Integro-differential Lugiato–Lefever model

We consider an optical cavity filled with a Kerr dispersive medium and driven by a coherent plane wave field, cf. Fig. I. Considering the Kerr effect and chromatic dispersion, light propagation in the cavity is governed by the nonlinear Schrodinger equation (NLSE)

$$\frac{\partial F}{\partial z} = i\beta_2 \frac{\partial^2 F}{\partial \tau^2} + i\gamma|F|^2 F, \quad (1)$$

where  $F$  is the slowly varying electric field envelope,  $z$  is the longitudinal coordinate along the propagation axis,  $\tau$  is the time in a reference frame traveling at the group velocity of light in the Kerr material. We assume that the cavity operates with anomalous dispersion, assuming that the dispersion coefficient  $\beta_2$  is positive. The nonlinear coefficient  $\gamma = 2\pi n_2/\lambda_0$  with  $n_2$  the nonlinear refractive index and  $\lambda_0$  is the light wavelength in the vacuum.

In addition to the effects of dispersion and non-linearity, the field propagating inside the cavity undergoes coherent superposition with the input light beam at the cavity's input beam splitter. The cavity boundary conditions describe this process

$$F^{p+1}(0, z) = \theta F_i + \rho \exp(i\phi) h \otimes F^p(l, z), \quad (2)$$

where  $\rho$  and  $\theta$  are the reflection and transmission coefficients at the output and the input beam splitter. The above equation provides a relation between the intracavity field envelope  $F^{p+1}$  at the input of the cavity after the  $p + 1$ -th round-trip and the field  $F^p(l, z)$  at the output after the  $p$ -th pass in the cavity, where  $l$  is the cavity length. The phase  $\phi = 2\pi nl/\lambda_0$  represents the linear phase accumulated by the field during a round-trip time,  $t_r$ , with  $n$  as the refractive index. The evolution of the intracavity field is thus slow over the time scale of the order  $t_r$ . In Eq. (2), the symbol  $\otimes$  denotes the convolution between the intracavity field  $F^p$  after  $p$  round-trip and the filter transfer function  $h$ .

The nonlinear Schrödinger Eq. (1) supplemented by the cavity boundary conditions, Eq. (2), constitutes an infinite dimensional map. To simplify the theoretical analysis of the problem, it is convenient to reduce this map to a single integrodifferential equation.

The temporal evolution can be considered continuous by replacing the map index  $p$  with a slow time scale  $t$  to model the evolution of the field envelope at the cavity entrance, i.e., the point  $z = 0$ . This can be achieved by defining the continuous variable  $F(t, \tau)$  as the intracavity field envelope at  $z = 0$ , and continuous slow time  $t = pt_r$  as

$$F(t = pt_r, \tau) = F(t, \tau) = F^p(z = 0, \tau), \quad (3)$$

where  $p$  is a positive integer number. The time  $t$  describes the slow evolution of the intracavity field from one round trip to another, while the structure of the intracavity field changes at the fast time scale  $\tau$ . The slow-time derivative can be defined as

$$t_r \frac{\partial F(t = pt_r, \tau)}{\partial t} = F^{p+1}(z = 0, \tau) - F^p(z = 0, \tau). \quad (4)$$

The injected field is coupled to the cavity only if the system is close to resonance. This means that the intracavity field does not vanish when the system operates close to resonance where the phase shift  $\phi$  is close to  $2\pi$ .

By averaging the right-hand side of the NLSE Eq. (1) over one cavity length, we get

$$\begin{aligned} F^p(l, \tau) &= F^p(0, \tau) + i\frac{\beta_2 l}{2} \frac{\partial^2 F^p(0, \tau)}{\partial \tau^2} \\ &+ i\gamma l |F^p(0, \tau)|^2 F^p(0, \tau). \end{aligned} \quad (5)$$

By taking into account both continuous-time Eq. (3), i.e.,  $F^p(0, \tau) = F(t, \tau)$  and its derivative Eq. (4), i.e.,  $\partial_t F(t = pt_r, \tau) = \partial_t F(t, \tau)$ , and by replacing the field amplitude  $F^p(l, \tau)$  that appear in Eq. (5) in the boundary conditions Eq. (4), we obtain

$$\begin{aligned} t_r \frac{\partial F(t, \tau)}{\partial t} &= \theta F_i - F(t, \tau) + \rho \exp(i\phi) \left[ h \otimes F(t, \tau) \right. \\ &+ \frac{i\beta_2 l}{2} h \otimes \frac{\partial^2 F(t, \tau)}{\partial \tau^2} \\ &\left. + i\gamma l h \otimes |F(t, \tau)|^2 F(t, \tau) \right]. \end{aligned} \quad (6)$$

This equation is an integrodifferential equation containing three convolution terms obtained from an infinite-dimensional map Eqs. (1, 2) by averaging over a cavity length and by introducing a continuous time and its derivative.

### B. Mean-field approximation: the Lugiato–Lefever model with spectral filtering

To describe the evolution of the intracavity field, we use the mean-field approach to further simplify the integrodifferential equation Eq. (6) into a partial differential equation. Before applying the mean-field approximation, let us first evaluate the three convolutions that appear in Eq. (6). The term  $h \otimes F(l, \tau)$  is given by

$$h \otimes F = \int \mathcal{F}[h_r + ih_i] F(t - \tau) d\tau, \quad (7)$$

where the complex filter transfer function in the frequency space  $h = h_r + ih_i$ , and  $\mathcal{F}$  is the Fourier transform

$$\mathcal{F}[h_r + ih_i] = \frac{1}{2\pi} \int \exp(-i\omega\tau) [h_r(\omega) + ih_i(\omega)] d\omega. \quad (8)$$

Expanding the term  $F(t - \tau)$  in a Taylor series, one gets

$$\begin{aligned} h \otimes F &= \int (\mathcal{F}[h_r] + i\mathcal{F}[h_i]) \sum_{n=0}^{\infty} (-1)^n \frac{\tau^n}{n!} \frac{\partial^n F(t)}{\partial \tau^n} d\tau, \\ &= \sum_{n=0}^{\infty} a_n \frac{\partial^n F}{\partial \tau^n} + i \sum_{n=0}^{\infty} b_n \frac{\partial^n F}{\partial \tau^n}, \end{aligned} \quad (9)$$

the coefficients  $a_n$  and  $b_n$  are

$$a_n = (-1)^n \int \mathcal{F}[h_r(\tau)] \frac{\tau^n}{n!} d\tau, \quad (10)$$

$$b_n = (-1)^n \int \mathcal{F}[h_i(\tau)] \frac{\tau^n}{n!} d\tau. \quad (11)$$

The above coefficients are well-defined for functions  $\mathcal{F}[h(\tau)]$  that decay faster than a polynomial. Our analysis until now is general; we do not specify the temporal shape of the filter transfer function. If we assume that the real and imaginary parts of  $h$  are an odd and even function of frequency, then  $a_{2n+1} = 0$  and  $b_{2n} = 0$ . Given this restriction, the first-order expansion in  $n$  yields

$$h \otimes F = (h_r + ih_i) \otimes F \approx a_0 F + a_2 \frac{\partial^2 F}{\partial \tau^2} + ib_1 \frac{\partial F}{\partial \tau}. \quad (12)$$

A similar calculation leads to the evaluation of the two other convolutions in the integrodifferential Eq. (6), namely

$$h(\omega) \otimes \frac{\partial^2 F}{\partial \tau^2} \approx c_0 \frac{\partial^2 F}{\partial \tau^2} + ic_1 \frac{\partial^3 F}{\partial \tau^3}, \quad (13)$$

$$h(\omega) \otimes |F|^2 F \approx d_0 |F|^2 F + id_1 \frac{\partial |F|^2 F}{\partial \tau}. \quad (14)$$

By replacing the three convolution terms Eqs. (12,13,14) in the integrodifferential equation Eq. (6), and applying the mean-field approximation consisting of the following assumptions: (i) We restrict our analysis to high-finesse cavities. This means that the transmission coefficient  $\theta$  is assumed to be much smaller than unity  $\theta \ll 1$ , so that the reflection coefficient is  $\rho \approx 1 - \theta^2/2$ , (ii) the linear phase shift acquired by the light is small  $\phi \ll 1$  over length  $l$ , so that  $\exp(i\phi) \approx (1 + i\phi)$ , (iii) the nonlinear phase shift must be smaller than unity, i.e.,  $\gamma l |F|^2 \ll 1$ . (iv) The cavity length is much shorter than the characteristic dispersion length of the field. Under these approximations, the integrodifferential equation (6) leads to a partial-differential equation often referred to as the generalized Lugiato–Lefever equation (GLLE):

$$\begin{aligned} t_r \frac{\partial F}{\partial t} &= \theta F_i - F + \left(1 - \frac{\theta^2}{2} - i\phi\right) a_0 F \\ &+ \frac{a_2}{2} \frac{\partial^2 F}{\partial \tau^2} + ib_1 \frac{\partial F}{\partial \tau} + \frac{i\beta_2 l}{2} \left[ c_0 \frac{\partial^2 F}{\partial \tau^2} + ic_1 \frac{\partial^3 F}{\partial \tau^3} \right] \\ &+ i\gamma l \left[ d_0 |F|^2 F + id_1 \frac{\partial |F|^2 F}{\partial \tau} \right]. \end{aligned} \quad (15)$$

This mean-field equation is quite general in that we do not explicitly specify the form of the transfer function of the filter; we simply require that the real part of the  $h(\omega)$  function be an odd function and the imaginary part an even function of

frequency. More specifically, let us consider the higher-order Lorentzian filter [30], [31]

$$h_r(\omega) = \frac{ba^4}{(\omega - \omega_f)^4 + a^4}, \quad (16)$$

$$h_i(\omega) = \frac{ab(\omega - \omega_f)[(\omega - \omega_f)^2 + a^2]}{(\omega - \omega_f)^4 + a^4}, \quad (17)$$

where the parameters  $a$  and  $b$  are linked to the filter bandwidth and the filter strength, respectively.  $\omega_f$  denotes the frequency of the filter. We can further simplify the generalized mean-field LLE by assuming that the filter bandwidth is large  $a \gg 1$ , then the coefficient associated with the imaginary part of the filter transfer function in Eq. (15) appears in the second order, namely  $c_1 \ll 1$  and  $d_1 \ll 1$ . Under these approximations, the Eq. (15) becomes

$$\begin{aligned} t_r \frac{\partial F}{\partial t} &= \theta F_i - \left(1 - a_0 + \frac{\theta^2}{2} + i\phi a_0\right) F + i\gamma l d_0 |F|^2 F \\ &+ ib_1 \frac{\partial F}{\partial \tau} + \left(a_2 + \frac{i\beta_2 l c_0}{2}\right) \frac{\partial^2 F}{\partial \tau^2} \end{aligned} \quad (18)$$

To reduce the number of parameters describing the time evolution of the intracavity field, we introduce the following scaling and renormalization:

$$\begin{aligned} (E, E_i) &= (F, \theta F_i) \frac{\gamma l d_0}{1 - a_0}, \quad t \rightarrow \frac{\kappa}{t_r} t, \\ (\delta, \beta, \alpha_1, \alpha_2) &= (2a_0 \phi, \beta_2 l c_0, 2b_1, a_2) / 2\kappa, \\ \kappa &= 1 - a_0 + \theta^2/2. \end{aligned} \quad (19)$$

Under these changes, the generalized LLE Eq. (18) takes its dimensionless form

$$\begin{aligned} \partial_t E &= E_i - (1 + i\delta) E + i|E|^2 E \\ &+ i\alpha_1 \frac{\partial E}{\partial \tau} + (\alpha_2 + i\beta) \frac{\partial^2 E}{\partial \tau^2}, \end{aligned} \quad (20)$$

Taking into account the temporal or spatial filters associated with gain dispersion or diffusion, respectively, in the modeling of the ring cavity filled with Kerr media implies considering not only a diffusive term;  $\alpha_2 \partial_\tau^2 E$ ; as in [32], [33], [35], but also the first derivative whose coefficient is complex;  $i\alpha_1 \partial_\tau E$ .

### III. LINEAR STABILITY ANALYSIS AND MODULATIONAL INSTABILITY

#### A. Linear stability analysis

The homogeneous stable states (HSS) of Eq. (20) are  $E_i^2 = |E_s|^2 [1 + (|E_s|^2 - \delta)^2]$ . They are independent of the parameters  $\alpha_{1,2}$ , and the HSS are therefore unaffected by the spectral filtering effect. For  $\delta < \sqrt{3}$  ( $\delta > \sqrt{3}$ ), the transmitted intensity as a function of the input intensity  $E_i^2$  is monostable (bistable). With periodic boundaries, we consider small fluctuations  $\exp(\lambda_\omega t + i\omega\tau)$  around the homogeneous steady state  $E_s$ , where the frequency  $\omega$  verifies the relation  $(\partial_\omega^2 + \omega^2) \exp(i\omega\tau) = 0$ . This formulation leads to a characteristic equation which is quadratic in  $\lambda$  and whose coefficients are functions of  $\omega^2$  and the system parameters:

$$\begin{aligned} \lambda^2 &+ 2(1 + \alpha_1 \omega + \alpha_2 \omega^2) \lambda + (1 + \alpha_1 \omega + \alpha_2 \omega^2)^2 \\ &+ (2I_s - \delta - \beta \omega^2)^2 - I_s^2 = 0, \end{aligned} \quad (21)$$

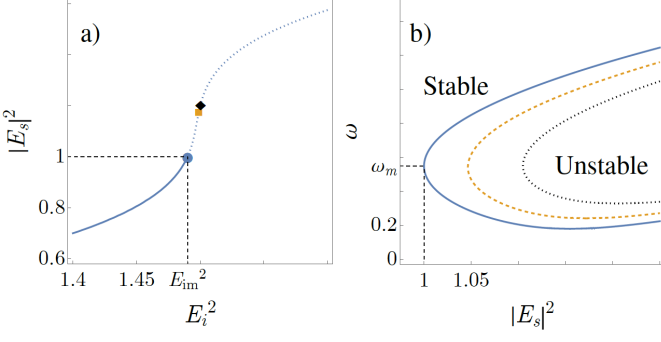


Fig. 2. a) Homogeneous steady states of Eq. (20) in the monostable case for anomalous dispersion where the threshold of the modulational instability is shown with markers for different values of  $\alpha_1 = \alpha_2 = \alpha$ . The blue dot corresponds to  $\alpha = 0$ , the orange square to  $\alpha = 0.05$ , and the black diamond to  $\alpha = 0.1$ . b) Marginal stability curve for the frequency as a function of the homogeneous steady state intensity. The blue full line corresponds to  $\alpha = 0$ ; the orange dashed line to  $\alpha = 0.05$ , and the black dotted line to  $\alpha = 0.1$ . Other parameters are  $\delta = 1.7$ ,  $\beta = 1$ .

where  $I_s = |E_s|^2$ . The solutions of this equation reads

$$\lambda_{1,2} = - (1 + \alpha_1 \omega + \alpha_2 \omega^2) \pm \sqrt{I_s^2 - (2I_s - \delta - \beta \omega^2)^2}. \quad (22)$$

In the Fourier space, unstable modes are characterized by a finite range of frequencies excluding the origin. This range must exclude all large periods (small frequency) corresponding to quasi-uniform distributions and very short periods (large frequency). They ensure that temporal fluctuations of arbitrarily small and large frequencies are damped. The well-known temporal modulational instability occurs when the eigenvalue corresponding to  $\omega_m$  changes sign and becomes positive. This dispersion relation determines the critical point associated with modulational instability provided that  $\lambda_\omega(\omega_m) = 0$  and  $\partial_\omega \lambda_\omega(\omega_m) = 0$ . The first condition leads to the marginal stability curve

$$(1 + \alpha_1 \omega + \alpha_2 \omega^2)^2 + (2I_s - \delta - \beta \omega^2)^2 = I_s^2. \quad (23)$$

In the absence of spectral filtering, i.e.,  $\alpha_1 = \alpha_2 = 0$ , we recover the well-known critical frequency and threshold for the modulational instability:  $|E_m|^2 = 1$  and  $\omega_m^2 = 2 - \delta$  obtained for  $\beta = 1$  [17]. When  $\alpha_1 \neq 0$  and  $\alpha_2 \neq 0$ , the threshold and critical frequency expressions at the modulation instability threshold are cumbersome. In the particular case,  $\alpha_1 = 0$

$$\omega_m^2 = \frac{\beta(2|E_m|^2 - \delta) - \alpha_2}{\alpha_2^2 + \beta^2}, \quad (24)$$

where  $|E_m|^2$  is the critical intensity at the onset of the bifurcation and is given by

$$|E_m|^2 = \frac{2\alpha_2 \pm (\alpha_2 \delta - \beta) \sqrt{\alpha_2^2 + \beta^2}}{3\alpha_2^2 - \beta^2}. \quad (25)$$

Let us first consider the anomalous dispersion regime where the chromatic dispersion coefficient is positive, i.e.,  $\beta > 0$  and focus on the monostable case where the output is a single-valued function of the injected field amplitude, i.e.,

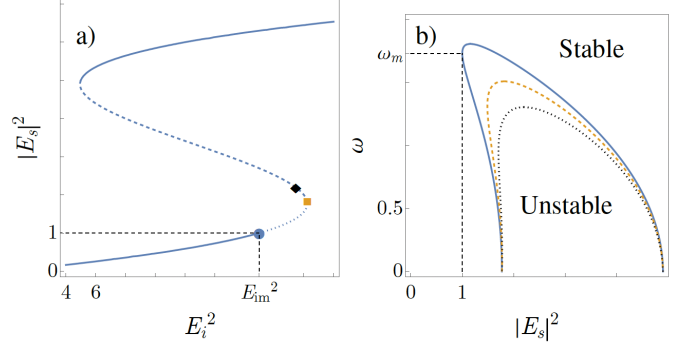


Fig. 3. a) Homogeneous steady states of Eq. (20) in the bistable case for normal dispersion where the threshold of the modulational instability is shown with markers for different values of  $\alpha_1 = \alpha_2 = \alpha$ . The blue dot corresponds to  $\alpha = 0$ , the orange square to  $\alpha = 0.05$ , and the black diamond to  $\alpha = 0.1$ . b) Marginal stability curve for the frequency as a function of the homogeneous steady state intensity. The blue full line corresponds to  $\alpha = 0$ ; the orange dashed line to  $\alpha = 0.05$ , and the black dotted line to  $\alpha = 0.1$ . Other parameters are  $\delta = 5$ ,  $\beta = -1$ .

$\delta < \sqrt{3}$ . Fig. 2 shows the input-output characteristics and the marginal stability curves for different values of  $\alpha_1$  and  $\alpha_2$ . The threshold associated with modulational instability is shifted towards a higher injected field strength, indicating that the spectral filter tends to stabilize the homogeneous steady states as shown in Fig. 2a).

The most unstable frequency becomes smaller as the  $\alpha_2$  parameter is increased, and obviously, the period of temporal structures emerging from the modulatory instability increases with the  $\alpha_2$  parameter, as shown in Fig. 2. In the monostable regime i.e.,  $\delta < \sqrt{3}$ , we see the threshold associated to the modulational instability is increased with the spectral filtering coefficients.

In the bistable regime, two intervals of the frequency detuning parameter are considered:

- When  $\sqrt{3} < \delta < -\alpha_2 + 2(\alpha_2^2 + 1)^{1/2}$ , a small portion of the lower homogeneous steady states is affected by the modulational instability (MI), namely in the range

$$|E_m|^2 < |E_s|^2 < \frac{\delta + \alpha_2}{2}, \quad (26)$$

For  $\delta = -\alpha_2 + 2(\alpha_2^2 + 1)^{1/2}$ , the MI threshold coincides with the lower limit point associated with bistability. The lower homogeneous state is unstable for all values of the input injection. Note that in the absence of spectral filtering, i.e., when  $\alpha_1 = \alpha_2 = \alpha = 0$ , we recover the frequency range for which a portion of unstable mode falls in the range  $\sqrt{3} < \delta < 2$ .

- When  $\delta > -\alpha_2 + 2(\alpha_2^2 + 1)^{1/2}$ , the lower homogeneous solution is stable, and the upper homogeneous steady state is always stable with respect to the modulational instability. Figure 3b) shows the marginal stability curve for this regime.

In the normal dispersion regime where the chromatic dispersion coefficient is negative, i.e.,  $\beta < 0$ , the MI does not affect the monostable regime. However, in the bistable case, a small portion of the lower homogeneous steady states becomes modulational unstable. When increasing the strength of spectral

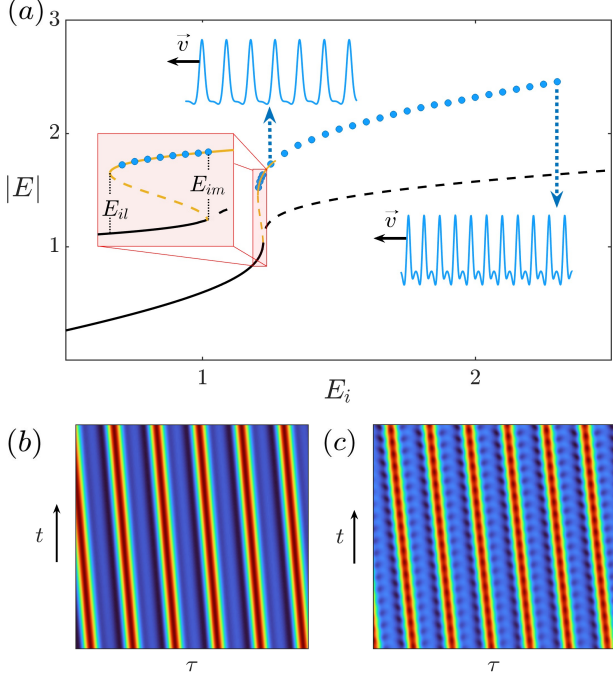


Fig. 4. Bifurcation diagram obtained in the monostable case. (a) The amplitude of the intracavity field as a function of the amplitude of the injected field. The black curve represents the CW solutions. The solid (dashed) line indicates stable (unstable) with respect to modulational instability. The blue dots indicate the maximum amplitude of moving periodic structures. The modulational instability appears to be subcritical. A hysteresis loop exists in the range  $E_{il} < E_i < E_{im}$  between stable CW solutions and moving periodic structures. A continuation algorithm generates the unstable and stable mustard curves resulting from the modulation instability, while the blue dots correspond to direct numerical simulations of Eq. (20). (b,c) The  $\tau$ – $t$  maps obtained for  $E_i = 2.3$  and  $E_i = 2.39$ , respectively, associated with regular moving periodic structures and breathing structures. Other parameters are  $\delta = 1.7$ ,  $\beta = 1$ ,  $\alpha_1 = 0.1$  and  $\alpha_2 = 0.1$ .

filtering, both states forming the hysteresis loop of the bistable output-input characteristics become modulationally stable, as shown in Fig. 3.

### B. Temporal periodic structures

As the input field increases, the flat solution becomes modulationally unstable, and the output field spontaneously develops a periodic structure with a well-defined frequency or period. This solution is of finite amplitude and is represented by full points in Fig. 4a). Using the implicit Euler algorithm scheme, they are obtained from numerical simulations of the mean-field model Eq. (20). Numerically, this is done using periodic boundary conditions compatible with the resonator geometry in Fig. I. The grid size is 500 with a temporal step integration size of 0.1. We consider the monostable regime where the homogeneous steady state solutions (CW solution) is a single-valued function of the injection beam [see the black curve of Fig. 4a)]. This solution is stable until the threshold denoted by  $E_i = E_{im}$ . Above this threshold, the CW solutions become unstable and develop spontaneously moving periodic structures. An example of this solution is plotted in the  $\tau$ – $t$  map in Fig. 4b). The amplitude of regular moving periodic solutions as a function of the input amplitude is indicated

by blue dots in the bifurcation diagram of Fig. 4a). When the input field intensity is decreased, the periodic solution remains stable even for  $E_i < E_{im}$ . These traveling solutions are stable in the subcritical domain, typically in the range of  $E_{il} < E_i < E_{im}$  as shown in Fig. 4a). The branch of moving periodic solution emerges from the modulational instability and is connected to the CW solution by unstable solutions represented by a dashed line as shown in the zoom of Fig. 4a). These unstable and stable branches of solutions are obtained by the pseudo-arc length continuation method, which allows the plotting of both stable and unstable periodic traveling solutions (mustard curves). As the input field is increased beyond the threshold of modulational instability, the output of the resonator evolves from regular to breathing self-pulsating structures. These solutions are moving with speed  $v$ . The  $\tau$ – $t$  map in Fig. 4c) shows examples of the temporal profiles of the breathing solutions. These solutions are moving with speed  $v$ , and their temporal profiles are shown in Fig. 4a). The motion is directly attributed to the presence of spectral filtering, which generates through mean-field modeling a term  $i\alpha_1\partial_\tau E$  in the generalized LLE model Eq. (20). From dynamical system theory, the presence of this term breaks the reflection symmetry  $\tau \rightarrow -\tau$  and makes the solution obviously moving. The existence of a parameter regime in which CW solutions coexist with a moving train of periodic solutions is a prerequisite for the formation of stable light confinement in optical resonators [36], which will be discussed in the next section.

## IV. DISSIPATIVE SOLITON COMBS WITH FILTERING

### A. Moving and Breathing Dissipative Soliton

Kerr micro- and macro-resonators support temporal dissipative solitons in the normal dispersion regime where the modulational instability appears subcritically. Their formation does not require a bistability between CW solutions. They can be generated in the monostable regime in the range  $\delta < \sqrt{3}$ . We consider the input field amplitude domain  $E_{il} < E_i < E_{im}$ , which gives rise to a hysteresis loop involving the CW solution and the traveling periodic solutions (see the zoom of Fig. 4a). As we shall see, different types of localized solutions exist as stable solutions associated with this domain. Numerical simulations of the generalized LLE model Eq. (20) show evidence of dissipative solitons. The results are summarized in Fig. 5. When  $\alpha = 0$ , LSs are stationary and symmetric solutions [see Fig. 5b)]. Their range of existence as stable solutions, indicated by full squares, is rather large, as shown in Fig. 5a). From this chart, we see that as the spectral filter parameters increase, the dissipative solitons stability range is reduced. In addition, we plot together with the points corresponding to the localized states for  $\alpha_1 = 0.1$ , the branch of the periodic solutions moving that connects to the CW solution by an unstable solution represented by a dotted line as shown in Fig. 5a). The branches of the periodic solutions in motion for  $\alpha = 0$  and  $\alpha = 0.05$  are not shown in Fig. 5a) for readability. The unstable and stable branches of the periodic solutions are obtained using the pseudo-arc length continuation method. The stable branch of the moving periodic

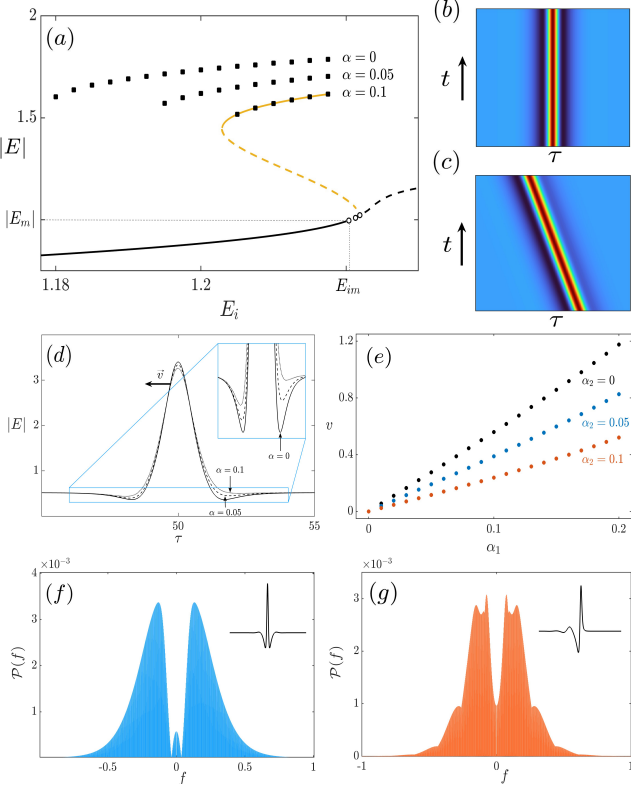


Fig. 5. Moving dissipative solitons obtained in the monostable case. (a) The maximum amplitude of the intracavity field associated with dissipative solitons as a function of the amplitude of the injected field. The black curve represents the CW solutions. As the input field increases, the CW solutions become unstable with respect to modulational instability. The black circles on this curve represent the threshold associated with modulational instability for  $\alpha = 0$ ,  $\alpha = 0.05$ , and  $\alpha = 0.1$ . The solid (dashed) line indicates stable (unstable) with respect to modulational instability. The three curves formed by black squares obtained for  $\alpha = 0$ ,  $\alpha = 0.05$  and  $\alpha = 0.1$  show the maximum amplitude of moving dissipative structures. (b) The  $\tau - t$  maps obtained for  $E_i = 1.21$ ,  $\alpha_1 = 0$ , and  $\alpha_2 = 0.1$  associated with stationary dissipative soliton. (b) The  $\tau - t$  maps obtained for  $E_i = 1.21$ ,  $\alpha_1 = 0.2$ , and  $\alpha_2 = 0.1$  associated with moving dissipative soliton. (d) A zoom-in on the dissipative solitons profile shows the deformation of the soliton tails for different values of the filter parameters. (e) The speed of dissipative solitons for a fixed amplitude of the injected field amplitude as a function of the parameter  $\alpha_1$ . (f,g) The combs associated with the stationary and moving dissipative solitons shown in (b) and (c), respectively. Other parameters are  $\delta = 1.7$ , and  $\beta = 1$ .

solution coincides with the localized branch of the solutions represented by the black dots. However, as we shall see, unlike the periodic solutions, the localized solutions branch is not connected to the CW solution.

In addition, when  $\alpha_1 \neq 0$ , the localized peaks become asymmetric and begin to exhibit regular motion, as shown in the  $\tau - t$  map in Fig. 5c). The profile of a single peak dissipative soliton is shown in Fig. 5d). The dissipative soliton has an exponentially decaying tail. As the parameter  $\alpha_1$  increases, the tail of the dissipative solitons becomes asymmetric due to the breaking of the  $\tau \rightarrow -\tau$  reflection symmetry of the system, as shown in the zoom of Fig. 5d). The motion is then due to the presence of temporal spectral filtering inside the cavity. The speed of single peak dissipative solitons as a function of the parameter  $\alpha_1$  is plotted in Fig. 5e). The speed increases with the parameter  $\alpha_1$  and decreases with  $\alpha_2$ . The Fourier transform

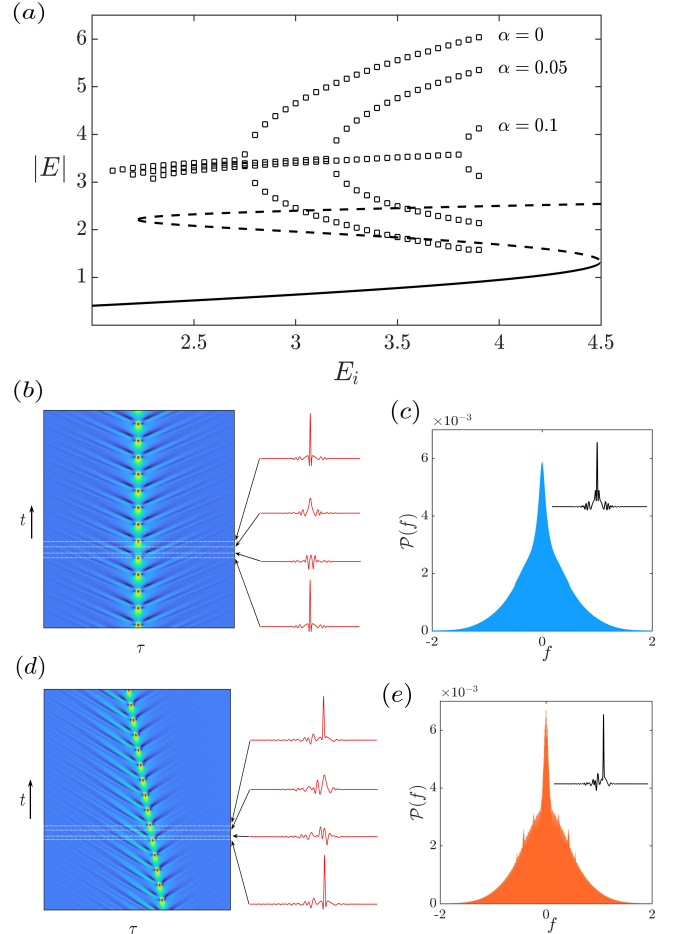


Fig. 6. Moving and breathing dissipative solitons obtained in the bistable case. (a) The maximum amplitude of the intracavity field associated with dissipative solitons as a function of the amplitude of the injected field. The black curve represents the CW solutions. The lower branch shown is always stable for  $\delta = 5$ , and the upper CW solution denoted by the dotted line is always unstable. The three curves formed by black squares obtained for  $\alpha_{1,2} = 0$ ,  $\alpha_{1,2} = 0.05$  and  $\alpha_{1,2} = 0.1$  show the maximum amplitude of moving dissipative structures. As the injected field amplitude is increased, the moving dissipative soliton branch exhibits a pitchfork bifurcation. Above this bifurcation, the DSs begin to breathe. The two branches emerging from this bifurcation represent the maximum and minimum amplitudes associated with the breathing dissipative solitons. (b) The  $\tau - t$  maps obtained for  $E_i = 3.9$ ,  $\alpha_{1,2} = 0$ , associated with breathing dissipative soliton. (d) The  $\tau - t$  maps obtained for  $E_i = 3.9$ ,  $\alpha_1 = 0.2$ , and  $\alpha_2 = 0.03$  associated with moving breathing dissipative soliton. (c,e) The combs associated with stationary and moving dissipative solitons are shown in (b) and (d), respectively. Parameters are  $\delta = 5$  and  $\beta = 1$ .

of the train of localized structures corresponding to Fig. 5b) and exiting the resonator is plotted in Fig. 5f). Similarly, the Fourier transform of the moving localized structures shown in 5c) is plotted in Fig. 5e). When the amplitude of the input field is increased in the monostable regime, localized breathing solutions are unstable because the background, the CW solution, becomes modulationally unstable.

We now consider the bistable regime  $\delta > \sqrt{3}$ . The linear stability analysis shows that the lower CW solutions become stable when considering spectral filtering. We fix the detuning parameter to  $\delta = 5$ , and we vary the input field amplitude. In the absence of spectral filtering  $\alpha_{1,2} = 0$ , numerical

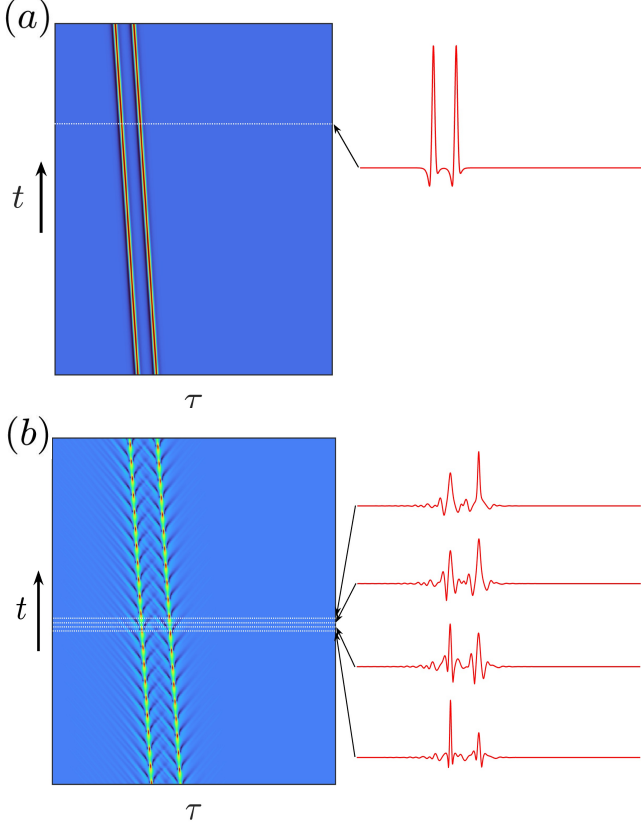


Fig. 7. Bounded dissipative solitons in the presence of spectral filtering. (a) bounded moving dissipative solitons and (b) bounded moving and breathing dissipative solitons obtained for the same parameters of Fig. 6b) and Fig. 6d), respectively.

simulations of the generalized LLE Eq. (20) show stationary dissipative solitons (the branch of open black squares in Fig. 6a). These regular dissipative solitons are stationary solutions similar to those shown in the monostable case [see Fig. 5b)]. When the input field is increased, DSs start to exhibit breathing behavior. An example is shown in Fig. 6b). The corresponding comb is plotted in Fig. 6c). When taking into account spectral filtering,  $\alpha \neq 0$ , the breathing solitons start to move with a constant speed as shown in Fig. 6d), and the corresponding combs are plotted in 6e).

Kerr micro- and macro-resonators can host bounded moving solutions. Fig. 7a) shows an example of two bounded moving dissipative solitons. Breathing and moving bounded dissipative solitons are also stable solutions of the generalized LLE model Eq. (20). This solution is shown in Fig. 7b). Dissipative solitons interact via their exponentially decaying tails and form bounded states. This weak interaction can be strongly affected by various perturbations, such as periodic modulation [37], [38] and high-order dispersions [28], [39]. These perturbations lead to the appearance of the so-called soliton Cherenkov radiation at the soliton tails [40], [41]. A deeper investigation of interaction in the presence of filtering will be the subject of future publication.

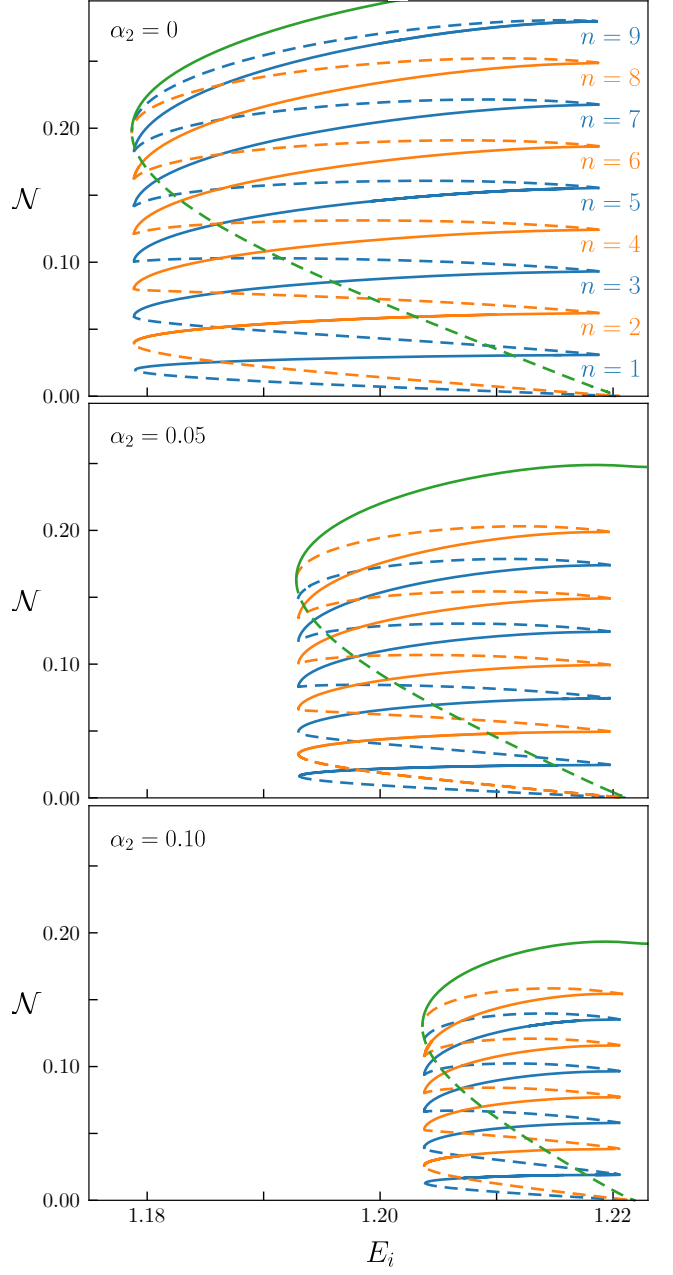


Fig. 8. Bifurcation diagram showing the L2-norm  $N = \int d\tau |E - E_s|^2$  as a function of the injection amplitude  $E_i$ . Green lines indicate periodic solutions, while (orange) blue lines indicate (even) odd numbers of peaks in localized states. Full (dashed) lines correspond to stable (unstable) states, respectively. Parameters are  $\delta = 1.7$ ,  $\beta = 1$ ,  $\alpha_1 = 0$ .

### B. Homoclinic snaking bifurcation and isolas of dissipative solitons

Kerr resonator exhibits a high degree of multistability over a finite range of injected field amplitude values, often referred to as the pinning region [42]. More precisely, the generalized LLE model Eq. (20) supports not only two peaks solutions bounded together but an infinite set of odd and even localized peaks. Let us first assume that  $\alpha_1 = 0$ , in this case, Eq. (20) admits a set of stationary solutions characterized by  $2n+1$  and  $2n$  peaks, where  $n$  is a positive integer. They are motionless

solutions when  $\alpha_1 = 0$  because the generalized LLE model Eq. (20) conserves the reflection symmetry  $\tau \rightarrow -\tau$ . Dissipative solitons exhibit a well-known homoclinic snaking type of bifurcation within the subcritical modulational instability range. In the time domain, their bifurcation diagram consists of two snaking curves that are connected and emerge from the modulational instability threshold [43], [44]. Since the maximum amplitudes of DSs with different numbers of peaks are close to each other, it is more convenient to plot the L2-norm

$$\mathcal{N} = \int d\tau |E - E_s|^2 \quad (27)$$

as a function of injected field amplitude. The homoclinic snaking bifurcation is shown in Fig. 8. The two snaking curves associated with odd and even numbers of localized peaks are intertwined. They correspond with the back-and-forth oscillations across the pinning region. This feature has been abundantly addressed for the Lugiato–Lefever model without spatial filtering. However, when  $\alpha_1 \neq 0$ , the classic homoclinic snaking type of bifurcation is broken, and a branch of one or more localized peaks forms an isolated stack. This means that the unstable branch associated with the dissipative soliton is not connected to the modulational instability threshold. This property is inherent to all irreversible systems in which the reflection symmetry is broken, i.e.,  $(\tau \not\rightarrow -\tau)$ . The summary of this analysis is shown in Fig. 9). The bifurcation diagram for moving periodic solutions and a dissipative soliton with a single peak is shown in Fig. 9a). The speed of a dissipative soliton is shown in Fig. 9b). Profiles corresponding to the points A-D along the isola branch shown in Fig. 9c) are indicated in the bottom left corner.

LLE Eq. (20) without the effect of spectral filtering is known to present a homoclinic snaking bifurcation diagram. However, taking spectral filtering into account, the first  $i\alpha_1\partial_\tau E$  derivative term in Eq. (20) is unavoidable, leading the homoclinic snaking bifurcation to be broken and the dissipative solitons to become asymmetric and exhibit motion. According to dynamical systems theory, this behavior is similar to the situation where considering the odd order of dispersion of Raman scattering leads to isolas [45], [46].

## V. CONCLUSIONS

We have studied the temporal formation of dissipative solitons and the corresponding combs generation in driven resonators under the combined influence of the Kerr effect, dispersion, dissipation, and spectral filtering. We have generalized the well-known mean-field Lugiato–Lefever model. The equation was derived from the infinite-dimensional Ikeda map with a general filter transfer function. It has been shown that in addition to the second-order derivative with a fast response time associated with the gain dispersion, an additional first-order derivative with a purely imaginary coefficient is necessary for the modeling. This term has a significant impact on the dynamics and results in the following consequences.

- The CW solutions stabilize the modulational instability by shifting it to higher intensity. Numerical simulations generate moving and breathing patterns. A branch of

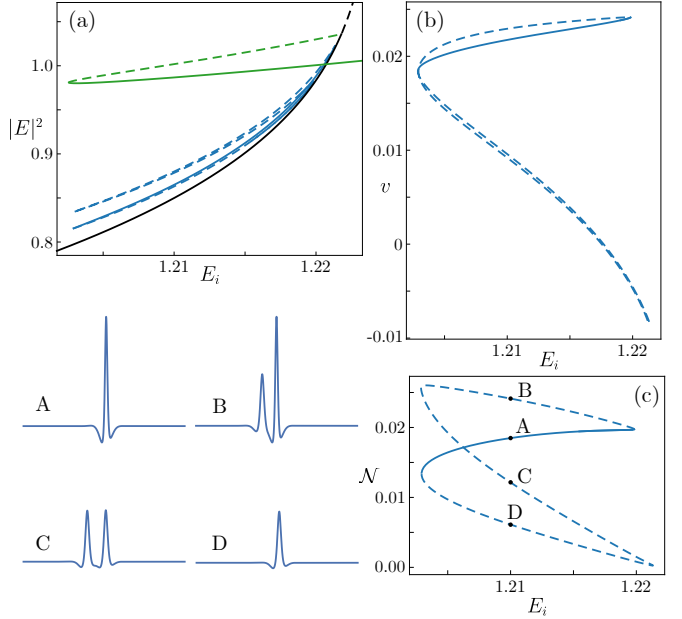


Fig. 9. Dissipative solitons isolas. (a) Bifurcation diagram showing the intensity of the intracavity field as a function of the injected field amplitude  $E_i$ . Black lines indicate the homogeneous steady state, green lines indicate the intensity of moving periodic solutions, and blue lines indicate the one-peak dissipative soliton. (b) Velocity of moving dissipative solitons isolas as a function of the injected field amplitude  $E_i$ . Full (dashed) lines correspond to stable (unstable) states, respectively. (c) L2-norm of the dissipative soliton branch as a function of the injected field amplitude. Insets A–D on the left show the profiles along the soliton branch. Parameters are  $\delta = 1.7$ ,  $\beta = 1$ , and  $\alpha_1 = \alpha_2 = \alpha = 0.1$ .

moving solutions connecting these periodic solutions to the modulational instability has been constructed using a continuation algorithm.

- It has been shown that the simple first derivative term not only breaks the reflection symmetry that causes dissipative solitons to move but also stabilizes the formation of moving dissipative solitons. In the monostable regime, where the CW solutions are single-valued functions of the injection field, we have shown that the stability domain of moving dissipative solitons is reduced by the spectral filtering.
- In the bistable regime, it has been demonstrated that spectral filtering increases the stability domain of regular moving dissipative solitons and moves the transition to breathing dissipative solitons to higher injected field amplitude. Numerical simulations have revealed the existence of moving-bounded dissipative solitons, including moving-breathing bounded dissipative solitons.
- The system's reflection symmetry is broken, which permits the formation of isolas dissipative solitons. In the absence of the first derivative, the system possesses reflection symmetry, and the bifurcation diagram comprises two snaking curves that are intertwined. These curves correspond to different numbers of peaks that are bound together.

## ACKNOWLEDGMENTS

M.B.G and M.G.C. acknowledge the financial support of ANID-Millennium Science Initiative Program-ICN17\_012 (MIRO) and FONDECYT project 1210353. M.T. is a Research Director at Fonds de la Recherche Scientifique FNRS.

## VI. REFERENCES SECTION

### REFERENCES

- [1] A. Pasquazi et al., Micro-combs: A novel generation of optical sources, *Physics Reports*, 729, 1, (2018).
- [2] T. Fortier, E. Baumann, 20 years of developments in optical frequency comb technology and applications. *Commun. Phys.* 2019, 2, 153 (2019).
- [3] N. Picqué, T.H. Hänsch. Frequency comb spectroscopy, *Nat. Photon.*, **13**, 146 (2019).
- [4] T.H. Hänsch, Nobel lecture: passion for precision, *Reviews of Modern Physics*, 78, 1297 (2006).
- [5] Herr, T., Brasch, V., Jost, J. D., Wang, C. Y., Kondratiev, N. M., Gorodetsky, M. L., Kippenberg, T. J. Temporal solitons in optical microresonators. *Nat. Photon.* **8**, 145 (2014).
- [6] Kippenberg, T. J., Gaeta, A. L., Lipson, M., Gorodetsky, M. L. Dissipative Kerr solitons in optical microresonators. *Science* **361**, 6402 (2018).
- [7] P. Del'Haye, A. Schliesser, O. Arcizet, T. Wilken, R. Holzwarth, T.G. Kippenberg. Optical frequency comb generation from a monolithic microresonator. *Nature*, 450(7173), 1214 (2007).
- [8] S.B. Papp, K. Beha, P. Del'Haye, F. Quinlan, H. Lee, K.J. Vahala, S. A. Diddams. Microresonator frequency comb optical clock. *Optica*, 1(1), 10(2014).
- [9] M.G. Suh, K.J. Vahala. Soliton microcomb range measurement. *Science*, 359(6378), 884 (2018).
- [10] Spencer et al. An optical-frequency synthesizer using integrated photonics. *Nature*, 557(7703), 81 (2018).
- [11] B. Min L. Yang, K. Vahala. Controlled transition between parametric and Raman oscillations in ultrahigh-Q silica toroidal microcavities. *Appl. Phys. Lett.* **87**, 181109 (2005).
- [12] W. Liang, V. Ilchenko, A. Savchenkov, A. Matsko, D. Seidel, L. Maleki. Passively Mode-Locked Raman Laser. *Phys. Rev. Lett.* **105**, 143903 (2010).
- [13] M. Karpov, H. Guo, A. Kordts, V. Brasch, M.H.P. Pfeiffer, M. Zervas, M. Geiselmann, T.J. Kippenberg. Raman self-frequency shift of dissipative Kerr solitons in an optical microresonator. *Phys. Rev. Lett.* **116**, 103902 (2016).
- [14] X. Liu, C. Sun, B. Xiong, L. Wang, J. Wang, Y. Han, Z. Hao, H. Li, Y. Luo, J. Yan, H.X. Tang. Integrated High-Q Crystalline AlN Microresonators for Broadband Kerr and Raman Frequency Combs. *ACS Photonics* **5**, 1943 (2018).
- [15] A. Chen-Jinnai, T. Kato, S. Fujii, T. Nagano, T. Kobatake, T. Tanabe. Broad bandwidth third-harmonic generation via four-wave mixing and stimulated Raman scattering in a microcavity. *Opt. Express* **24**, 26322 (2016).
- [16] S. Zhu, L. Shi, L. Ren, Y. Zhao, B. Jiang, B. Xiao, X. Zhang. Controllable Kerr and Raman-Kerr frequency combs in functionalized microsphere resonators. *Nanophotonics*, **8**, 2321 (2019).
- [17] L. A. Lugiato and R. Lefever. *Phys. Rev. Lett.* 58, 2209 (1987).
- [18] Y. K. Chembo, D. Gomila, M. Tlidi, and C. R. Menyuk, The European Physical Journal D 71, 198 (2017).
- [19] Scroggie, A. J., Firth, W. J., McDonald, G. S., Tlidi, M., Lefever, R., Lugiato, L. A. Pattern formation in a passive Kerr cavity. *Chaos, Solitons & Fractals* **4**, 1323 (1994).
- [20] Tlidi, M., Mandel P. & Lefever, R. Localized structures and localized patterns in optical bistability. *Phys. Rev. Lett.* **73**, 640 (1994).
- [21] A.B. Matsko, A. A. Savchenkov, W., Liang, V. Ilchenko, D. Seidel, L. Maleki, Mode-locked Kerr frequency combs. *Opt. Lett.* 36, 2845 (2011).
- [22] S. Coen, H.G. Randle, T. Sylvestre, M. Erkintalo. Modeling of octave-spanning kerr frequency combs using a generalized mean-field Lugiato-Lefever model. *Opt. Lett.* 38, 37 (2013).
- [23] L.A. Lugiato, F. Prati, M. Gorodetsky, T.J. Kippenberg. From the Lugiato-Lefever equation to microresonator-based soliton Kerr frequency combs. *Phil. Trans. R. Soc. A* 376, 20180113 (2018).
- [24] M. Tlidi, M. Clerc, and K. Panajotov, Dissipative structures in matter out of equilibrium: from chemistry, photonics and biology, the legacy of ilya prigogine (part 1), *Philos. Trans. R. Soc., A* 376, 20180114 (2018).
- [25] M.G. Clerc, S. Coulibaly, M. Tlidi. Time-delayed nonlocal response inducing traveling temporal localized structures. *Phys. Rev. Research* **2**, 013024 (2020).
- [26] M.G. Clerc, S. Coulibaly, P. Parra-Rivas, M. Tlidi. Non-local Raman response in Kerr resonators: Moving temporal localized structures and bifurcation structure, *Chaos* **30**, 083111 (2020).
- [27] P. Parra-Rivas, S. Coulibaly, M.G. Clerc, M. Tlidi. Influence of stimulated Raman scattering on Kerr domain walls and localized structures. *Phys. Rev. A* **103**, 013507 (2021).
- [28] M. Tlidi, L. Bahloul, L. Cherbi, A. Hariz, and S. Coulibaly, Drift of dark cavity solitons in a photonic-crystal fiber resonator, *Phys. Rev. A* 88, 035802 (2013).
- [29] M. Tlidi, A.G. Vladimirov, P. Pieroux, D. Turaev. Spontaneous motion of cavity solitons induced by a delayed feedback, *Phys. Rev. lett.* 103, 103904 (2009).
- [30] F. Bessin, A.M. Perego, K. Staliunas, S.K. Turitsyn, A. Kudlinski, M. Conforti, A. Mussot, Gain-through-filtering enables tuneable frequency comb generation in passive optical resonators. *Nature communications*, 10, 4489 (2019).
- [31] A.M. Perego, A. Mussot, M. Conforti, *Phys. Rev. A* 58, 2209 (2021).
- [32] X. Dong , S. Christopher, V.G. Bucklew, H.W. Renninger, Chirped-pulsed Kerr solitons in the Lugiato-Lefever equation with spectral filtering *Phys. Rev. Research* 3, 033252 (2021).
- [33] A. Pimenov, A.G. Vladimirov, Temporal solitons in an optically injected Kerr cavity with two spectral filters, *Optics* 3.4, 364 (2022).
- [34] A. G. Vladimirov and D. A. Dolinina. Neutral delay differential equation model of an optically injected Kerr cavity, *Phys. Rev. E* 109, 024206 (2024).
- [35] D. Turaev, A. G. Vladimirov, and S. Zelik. Long Range Interaction and Synchronization of Oscillating Dissipative Solitons, *Phys. Rev. Lett.* 108, 263906 (2012).
- [36] U. Bortolozzo, M. G. Clerc, and S Residori. Solitary localized structures in a liquid crystal light-valve experiment, *New J. Phys.* 11, 093037 (2009).
- [37] J. M. Soto-Crespo, N. N. Akhmediev, P. Grelu, and F. Belhache. Quantized separations of phase-locked soliton pairs in fiber lasers. *Opt. Lett.* 28, 1757 (2003).
- [38] M. Olivier, V. Roy, and M. Piché, *Opt. Lett.* 31, 580 (2006).
- [39] A. G. Vladimirov, M. Tlidi, and M. Taki, Dissipative soliton interaction in Kerr resonators with high-order dispersion *Phys. Rev. A* 103, 063505 (2021)
- [40] N. N. Akhmediev and M. Karlsson, Cherenkov radiation emitted by solitons in optical fibers. *Phys. Rev. A* 51, 2602 (1995).
- [41] A. G. Vladimirov, S. V. Gurevich, and M. Tlidi, Effect of Cherenkov radiation on localized-state interaction, *Phys. Rev. A* 97, 013816 (2018).
- [42] Y. Pomeau, *Physica D* 23, 3 (1986).
- [43] M. Tlidi, L. Gelens, High-order dispersion stabilizes dark dissipative solitons in all-fiber cavities, *Opt. Lett.*, 35, 306 (2010).
- [44] P. Parra-Rivas, D. Gomila, M.A. Matias, S. Coen, L. Gelens. Dynamics of localized and patterned structures in the Lugiato-Lefever equation determine the stability and shape of optical frequency combs, *Phys. Rev. A* 89 (4), 043813 (2014).
- [45] P. Parra-Rivas, D. Gomila, F. Leo, S. Coen, S., L. Gelens, L. Third-order chromatic dispersion stabilizes Kerr frequency combs. *Opt. Lett.* 39, 2971 (2014).
- [46] M Tlidi, M Bataille-Gonzalez, MG Clerc, L Bahloul, S Coulibaly, B Kostet, C Casillo-Pinto, K. Panajotov, Isolas of localized structures and Raman-Kerr frequency combs in micro-structured resonators. *Chaos, Solitons & Fractals* 174, 113808 (2023).